Electronic Supplementary Material (ESI) for Nanoscale.

Interfacial engineering to modulate surface dipoles, work functions and dielectric confinement of halide perovskites

Pooja Basera[1,2], Boubacar Traoré[1], Jacky Even[2],* and Claudine Katan[1]*

[1] *Univ Rennes, ENSCR, CNRS, ISCR - UMR 6226, F-35000 Rennes, France*

[2] *Univ Rennes, INSA Rennes, CNRS, Institut FOTON - UMR 6082, F-35000 Rennes, France*

E-mail: Jacky.Even@insa-rennes.fr; claudine.katan@univ-rennes1.fr

Supplemental Material

I. Computational details

The SIESTA code[2,3] based on a basis set of finite-range of numerical atomic orbitals is used for the DFT calculations[4,5]. The structural optimizations are performed using van der Waals density functional with C09 exchange[6] within the van der Waals DF2 flavor to describe the exchange-correlation term. The fast inertial relaxation engine (FIRE) algorithm[7] is used and the force tolerance has fixed to 0.02 eV/Å. We use the norm-conserving Troullier-Martins pseudopotentials[8] to take into account the core electrons for each atomic species. The valence electrons considered for H, C, N, Br, Pb, O and S are $1s^1$, $2s^2 2p^2$, $2s^2 2p^3$, $4s^2 4p^5$, $5d^{10} 6s^2 6p^2$, $2s^2 2p^4$ and $3s^2 3p^4$, respectively. A real space mesh grid energy cutoff of 350 Ry with the polarized double ζ basis set with an energy shift of 50 meV is used for the calculations. To describe accurately the properties of the surfaces, we include orbitals with weight in the vacuum region, known as diffuse orbitals[9]: diffuse orbitals (5s, 5p, 5d) for Br atom on the top two atomic layers on both sides of the slab with 30% diffuse orbital size or cutoff radii. A Monkhorst-Pack of $8\times8\times8$ and $4\times4\times1$ is used for the bulk and slab systems, respectively. Single point calculations are performed with PBE functional[10] including spin-orbit coupling (SOC) on top of vdwDF2-C09 optimized structures. Note that, SIESTA does not capture symmetries during geometry optimizations; thus, to circumvent this, the half-sum of the total charge densities across the slab in forward and reverse directions is taken. This results in more symmetrized density profiles.

The DFT optimized bulk structure of pseudo cubic $CsPbBr_3$ is used to construct the initial slabs. For surface layer relaxation of slabs, only the atomic positions are allowed to relax. We checked the convergence of number of octahedra layers to be relaxed at the surface. For this, we started with a 15 octahedra thick slab, and performed relaxation of 1 octahedra up to 6 octahedra layers on both sides of the slab, while keeping the internal layers frozen to mimic the bulk part of the slabs. Relaxation of two surface octahedra layers proves sufficient to reach converged surface dipole densities and valence energies. This ensures that our simulations do not induce an additional interface and related strain between the fixed and free regions of the slab. The total number of octahedra layers in the slab is also been varied from 1 to 10, and corresponding valence energies are shown in Fig S1. Beyond six octahedra, we observe a minimal change ($\sim$ 3.4 $\times 10^{-3}$ eV) in the valence energies (Fig S1a) and the position dependent high frequency dielectric profiles (Fig S1b). Thus, our pristine and functionalized slab models comprise a total of 8 octahedra, the two surface octahedra layers of the perovskite are allowed to relax, while the bulk like region is frozen and fixed to the relaxed bulk structure. We further computed the variations of valence energy and surface dipole densities obtained with and without fixing the bulk region of the slab, which amount to 0.06 eV and 0.07 x 10^{-11} C/m, respectively.

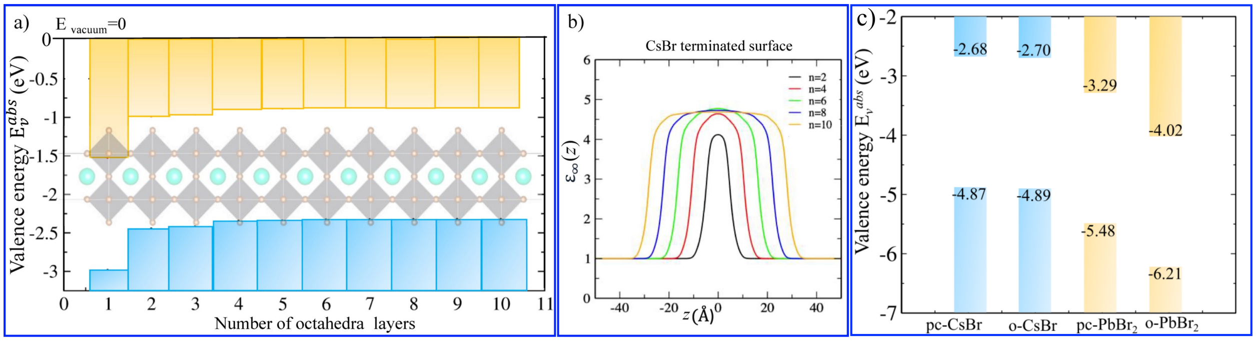

Figure S1: For CsBr terminated $CsPbBr_3$ slab a) Valence energy (E_v^{abs}) for octahedra layers varying from n= 1 to n=10. b) Position dependent high frequency dielectric profile for octahedra layers varying from n= 2 to n=10. c) Valence energies computed for pseudo cubic (pc-) and ortho (o-) slab crystal structures for CsBr and $PbBr_2$ terminated surfaces.

Besides, inorganic perovskite lattices tend to have lower symmetries, which affect how ligands relax on those surfaces along with the subsequent surface dipoles and valence energy levels. To address this, we compare the variations in valence energy (E_v^{abs}) (eV) due to changes in the crystal symmetry of $CsPbBr_3$ bulk section of the slab (Fig S1c). We observe almost negligible variation of E_v ($\sim$0.02 eV) when transitioning from pseudo cubic (pc-) to ortho (o-) in CsBr terminated surfaces ($\sim$0.02 eV), while a significant difference ($\sim$0.73 eV) is observed for $PbBr_2$ terminated ones. Consequently, the breaking of symmetry appears to have a more pronounced effect on E_v in $PbBr_2$ terminated surfaces. The changes in E_v^{abs} from pseudo cubic to ortho is related to how the octahedral distortions are affected at the surface. For $PbBr_2$ surface, the distortions are more pronounced in the ortho systems as compared to pseudo cubic one, resulting in a deeper valence energy. This can be attributed to the composition of the valence band maximum (VBM) in the perovskite, which involves anti-bonding hybridization between Pb(6s) and Br(4p) orbitals. However, it is important to note that our study specifically focuses on CsBr terminated surfaces, where both valence energies and octahedral distortions are minimally affected by the crystal symmetry of the bulk section of the layer.

For charge transfer, the electronic accumulation (depletion) upon the molecular adsorption is calculated by taking the charge density difference between the combined system and their individual counterparts. The expression for charge transfer from slab to adsorbate or vice-versa is given by:

$$\Delta\rho = \rho_{\text{slab+adsorb}} - (\rho_{\text{slab}} + \rho_{\text{adsorb}}) \tag{1}$$

where, $\rho_{\text{slab+adsorb}}$, ρ_{slab} , and ρ_{adsorb} are defined as the total electronic charge density of the whole system comprised of the perovskite slab and the adsorbate, the electronic charge density of the perovskite part of the slab, and the electronic charge density of the adsorbate, respectively. The positive and negative value of $\Delta\rho$ correspond to accumulation and depletion of electronic charge, respectively. Notably, in the SIESTA code, the positive and negative sign for charge density correspond to electronic charge density and ionic charge density, respectively.

I.1. Structural information

We use the pseudocubic for $CsPbBr_3$ for the dipole model to avoid issues related to symmetry breaking that could affect the model (proof of concept). The pseudo-cubic structure of $CsPbBr_3$ is obtained from its room temperature orthorhombic cell[11]. We determine the lattice constant of this pseudo-cubic structure using the relation:

$$a_{\text{pseudocubic}} = (V_{\text{ortho}}/4)^{1/3} \tag{2}$$

where V_{ortho} is the room temperature orthorhombic cell volume.

I.2. Comment on dipole corrections

In many cases, due to periodic boundary conditions along with asymmetric termination of slabs, an artificial electric field is generated across the slab. This can be inferred from the slope observed in the potential profile in the vacuum region of the slab. To circumvent this, a dipole correction scheme is often implemented that counterbalances the artificial electric field[12,13] and yields a flat potential in the vacuum region. This computational trick allows to determine the work functions for asymmetric surfaces. Here, we model our surface in such a way that the slope observed in the potential in the vacuum region is negligible due to the symmetrically terminated slabs. Hence, there is no need to use a dipole correction scheme. With the considered symmetric slab terminations, we verified that dipole correction has a negligible effect on the computed valence energies.

I.3. Band gap correction

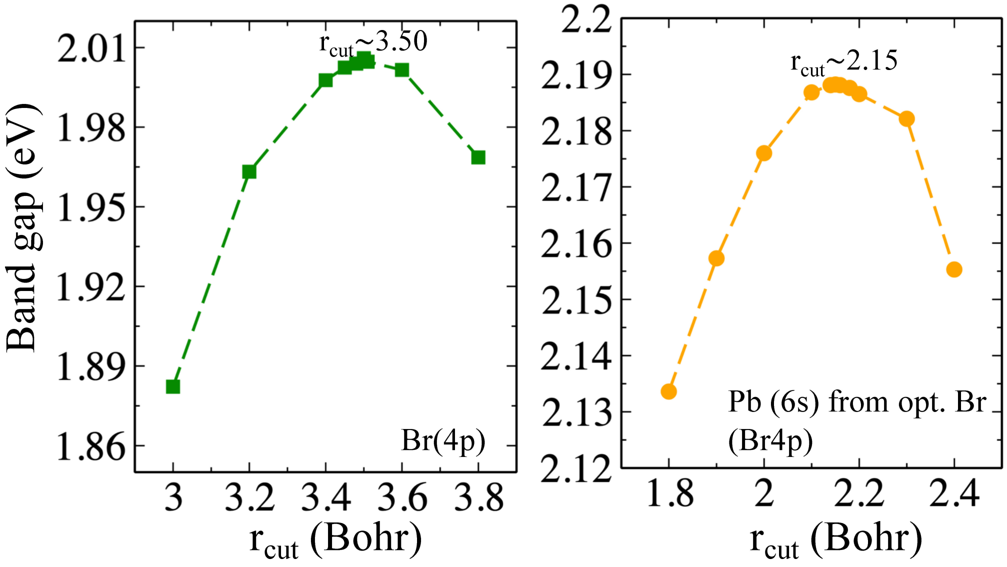

Figure S2: Optimizing r_{cut} for the pseudopotential of Br by removing 1/2 e^- from its 4p states (left panel). Right panel shows optimizing r_{cut} for the pseudopotential of Pb atom with the removal of 1/2e^- from its 6s states using the optimized Br(4p) atom from the left. The optimal r_{cut} are 3.50 Bohr and 2.15 Bohr for Br and Pb, respectively. Spin orbit coupling (SOC) effect is taken into account.

It is well known that DFT underestimates the band gap. In view of this, we use the Slater half-occupation technique implemented in DFT-$\frac{1}{2}$ i.e., PBE-$\frac{1}{2}$, to reach computed band gaps in better agreement with experimental ones[14–16]. Here, within PBE-$\frac{1}{2}$, we remove 1/2 electron from 4p and 6s orbitals of bromide (Br) and lead (Pb) atoms, respectively, because the valence band maximum of $CsPbBr_3$ perovskites is formed by an anti-bonding hybridization between Pb (6s) and bromide (4p) states[17]. Fig S2 shows the optimal r_{cut} values for Br and Pb that maximize the band gap of bulk $CsPbBr_3$. The obtained band gap from PBE-$\frac{1}{2}$ (with SOC) is 2.19 eV at the optimal r_{cut} for Br ($\sim$3.50 Bohr) and Pb ($\sim$2.15 Bohr + optimized r_{cut} from Br). The calculated band gap from PBE-$\frac{1}{2}$ (2.19 eV) is in fair agreement with the experimental value (2.25 eV[11]). We have used PBE-$\frac{1}{2}$ to align the CBM absolute energies (Fig 2b in main manuscript, and FigS11(b) and (d)). More details for PBE-$\frac{1}{2}$ is given in Ref.[16].

I.4. Hartree potential approach for valence energies

The valence energies, with absolute energy scale fixed with respect to the vacuum level, are computed using the method based on Hartree potential alignment[18,19].

$$\mathrm{E}_v^{abs}[HP] = \mathrm{VBM}_{bulk} + \Delta V_H + \Delta \mathrm{E}_{\mathrm{vacuum}} \tag{3}$$

where, VBM_{bulk} corresponds to valence band maximum of the bulk system, $\Delta V_H = V_H^{slab} - V_H^{bulk}$ is defined as the shift in the Hartree potential between the slab and the bulk systems, and $\Delta \mathrm{E}_{\mathrm{vacuum}} = 0 - \mathrm{E}_{\mathrm{vacumm}}$ is the shift in the vacuum level with respect to zero energy level.

II. Definition and convention

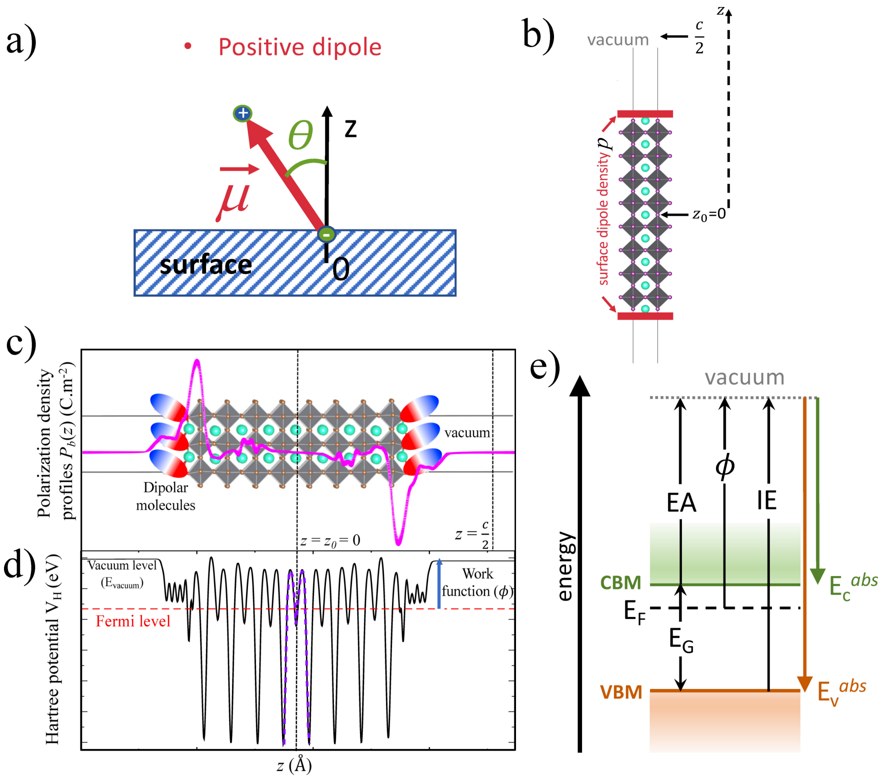

Figure S3: a) Convention used for positive dipoles: the dipole moment direction is from negative to positive charge. b) Constructed symmetric slab model, where $z = z_0 = 0$ (center of the slab) and $z = c/2$ (middle of the vacuum) and p is surface dipole density. c) Example of polarization density profile $P_b(z)$ shown in magenta color, plotted on top of the corresponding slab. d) Schematic of the Hartree potential profile used to compute the work function (ϕ) in the framework of *ab initio* calculations. A potential shift between the slab and the bulk resulting in superimposed profiles at the centre of the slab (bulk-like region) is used to obtain valence energies with respect to the vacuum level. e) Schematic illustration of the energy diagram of a semiconductor with band edges (VBM and CBM) and corresponding energies, fundamental energy gap (E_G), Fermi level (E_F), vacuum level, work function (ϕ), ionization energy (IE) and electron affinity (EA). The valence energy (E_v^{abs}) is defined on an absolute scale, i.e. with respect to the vacuum level. In the same way, the work function (ϕ) is defined with respect to the Fermi level. In the present work, we put the Fermi level at the top of the valence band and $\phi = -E_v^{abs}$.

III. Investigated ligands

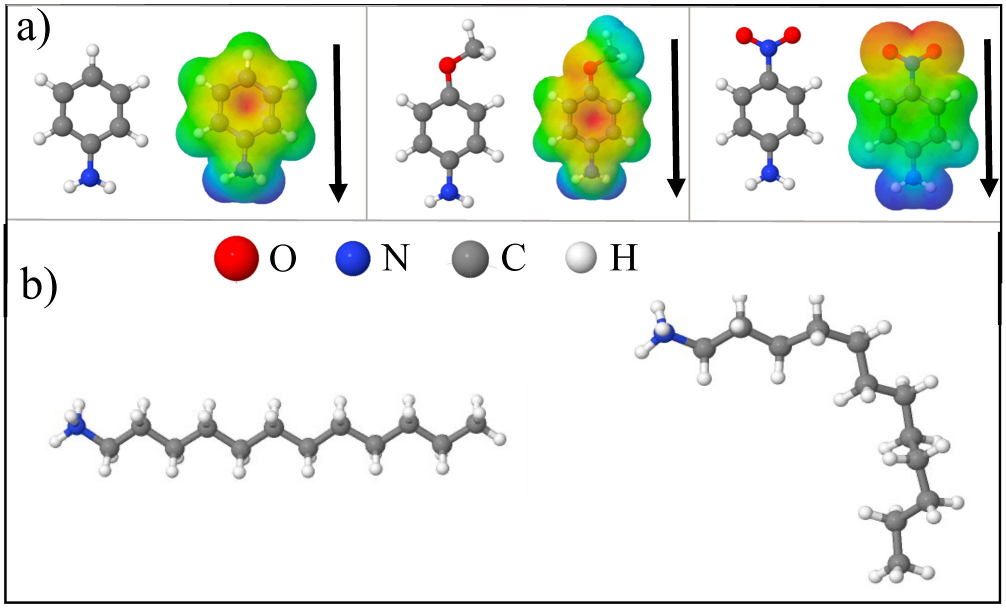

Figure S4: a) Aniline, Aniline$-$OCH$_3$, Aniline$-$NO$_2$, and their Hirshfeld charge analysis to show the direction of the dipole moment. The Red (blue) region corresponds to excess electronic charge (electron deficiency). Black arrows show the direction of the dipole moments. b) Comparison between the linear conformation obtained with DFT optimization of an isolated DA cation and the more realistic molecular conformation extracted from finite temperature classical MD simulations[20].

Investigated ligands are shown in Fig 1 and Fig S4. Depending on the molecule, different ways to functionalize the surface are considered. The DMSO molecule has a strong dipole and it is commonly used as a solvent in the fabrication of perovskite thin films[21,22]. In our functionalized slabs, we place the oxygen (O) atom of the DMSO molecule at the place of Br (outer terminal) atom. While doing so, the excess of negative charge occurs in the system, and for neutralizing that charge, we remove a Cs-atom in the vicinity of the surface, where the molecules are attached. This is consistent with experimentally reported adducts that have been observed during perovskite film fabrication.[23,24] We stress that this is only one of the possibilities. DMSO coud also bind just on top of the CsBr layer (with O-atom bound to Cs), and/or to other facets, such as (110) or (111) facets (referred to cubic structure), but these alternative situations are not investigated in the present study. Regarding acids that are often used for defect passivation, consistently with previously reported modeling strategies[25] we remove the H atom from the oleic and phosphonic acids ($-$OH end) and form the oleate and phosphonate anions, respectively. Then, we substitute a bromine (Br) atom (outer terminal) by the oxygen atom (O) of the anion. This ensures the charge neutrality of the whole system. For the aniline derivatives recently investigated in the context of solar cells,[1] the situation is less clear. In fact, there is no experimental information about their charge state nor orientation on the perovskite surface. Given the affinity between ammonium groups and halide perovskites, we first consider anilinium and its derivatives and place the nitrogen atom of the NH_3^+ group at the position of the Cs-atom of the outer layer of the $CsPbBr_3$ slab (Fig 3a) as proposed in Ref.[26,27]. We consider also the neutral molecules with the NH_2 group pointing towards the perovskite surface (Fig S16), as hypothesized in the original work[1]. For nitro-aniline, the NO_2 group may also point towards the surface (Fig S18) and we thus also considered this case. These various binding modes will lead not only to different surface relaxation, but also different charge transfer between ligand and surface, which in turn will modify the surface dipole density.

For the primary, secondary and quaternary alkylammonium ligands, initial structures (position and orientation of the ligands) are extracted from classical MD simulations.[20]. Note that, precise crystallographic data are lacking for these flexible molecules, not only regarding their average static conformations, but also to gauge the degree of dynamical disorder (partial atomic occupancies, Debye Waller factors, etc). We have therefore utilized snapshots from classical MD simulations to account for the numerous possibilities that arise due to the inherent flexibility of molecules with long chains as well as their disorder at room temperature. The authors of reference[20] showed that these snapshots better reflect the actual molecular bonds and subsequent distortions. These molecules have a distorted molecular backbone, as compared to the linear chain obtained with DFT optimization of an isolated molecule, as illustrated in Fig S4b.

Table S1 presents the variation in surface relaxation for same molecule with different molecular chain orientation i.e., one with DFT optimized linear chains and one starting from an MD snapshot. Based on Table S1, we deduce that molecular structures obtained from MD simulation lead to more reasonable distortions in the perovskite surface layers, characterized by larger in-plane Pb-Br-Pb angles and smaller out-of-plane delta angles.

Table S1: Average in-plane Pb-Br-Pb angle and out-of-plane (δ angle[28]), in-plane and out-of-plane PbBr bond lengths at the outermost surface layers of $CsPbBr_3$ slab functionalized with DA cation[20]. Subscripts "in" and "out" refer to the in-plane and out-of-plane, respectively.

	$PbBr_{in}$ (Å)	Pb-Br-Pb_{in} (°)	$PbBr_{out}$ (Å)	δ_{out} (°)
With DFT optimized linear chains	3.02	151.7	2.98	8.86
Starting from an MD snapshot	2.97	161.1	2.97	7.22

IV. Convergence of carbon chain length for the molecules on a $CsPbBr_3$ surface

Phosphonate anion:

Table S2: Surface dipole densities (p) and valence energies E_v^{abs} computed for phosphonate anions functionalizing a model $CsPbBr_3$ slab for various alkyl chain lenghts.

Alkyl chain length	p (C/m)	E_v^{abs} (eV)
1 carbon	3.37×10^{-11}	-3.50
2 carbons	3.38×10^{-11}	-3.54
3 carbons	3.37×10^{-11}	-3.50
4 carbons	3.36×10^{-11}	-3.49
5 carbons	3.42×10^{-11}	-3.54
6 carbons	3.44×10^{-11}	-3.54
7 carbons	3.46×10^{-11}	-3.54
8 carbons	3.42×10^{-11}	-3.54

Here, we vary the length of the carbon chain of the phosphonate anion to chose the minimal length needed to accurately compute surface dipole densities (p) and valence energies E_v^{abs} of $CsPbBr_3$ surfaces functionalized with phosphonate anions. Results are given in Table S2. From 1 to 4 carbons in the alkyl chain, the change in E_v^{abs} is $0.01-0.05$ eV. Beyond five carbons, the value saturates. Hence, to reduce the computational burden, we consider a 5 carbon chain length for the phosphonate anion.

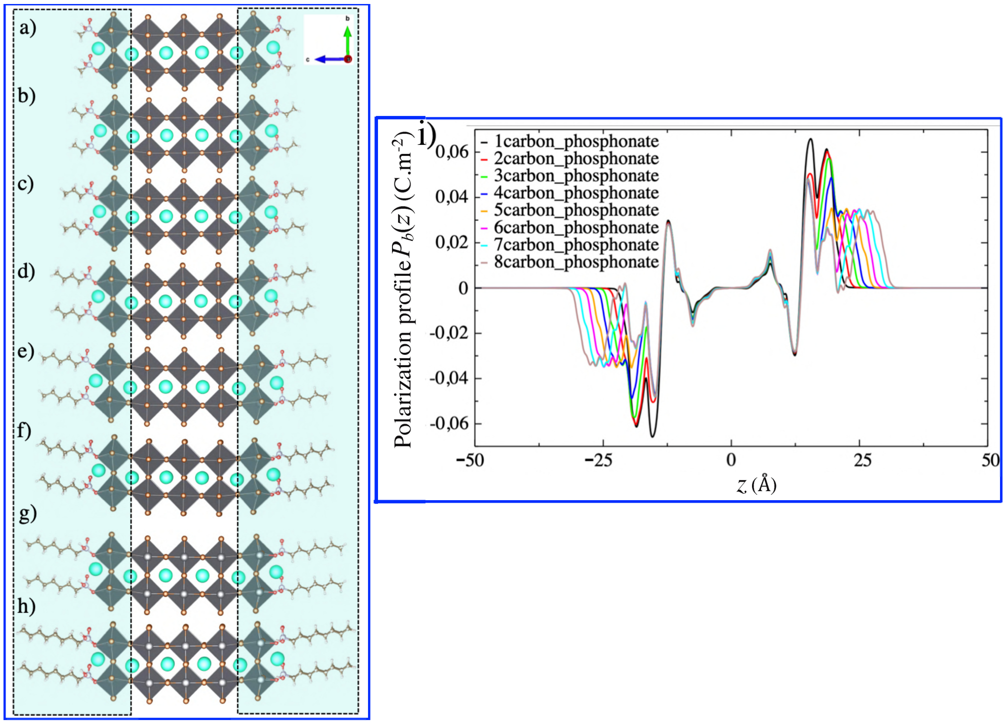

Figure S5: (a)-(h) Relaxed $CsPbBr_3$ model slabs functionalized with phosphonate anions bearing alkyl chains of various length: from $1-8$ carbons. (i) Corresponding polarization density profiles ($P_b(z)$).

Oleate anion:

Table S3: Surface dipole densities (p) and valence energies E_v^{abs} computed for oleate anions functionalizing a model $CsPbBr_3$ slab for various alkyl chain lenghts.

Alkyl chain length	p (C/m)
2 carbons	2.73×10^{-11}
3 carbons	3.03×10^{-11}
4 carbons	3.30×10^{-11}
5 carbons	3.42×10^{-11}
6 carbons	3.41×10^{-11}

Table S3 shows that 5 carbon atoms are also sufficient in the case of oleate anions.

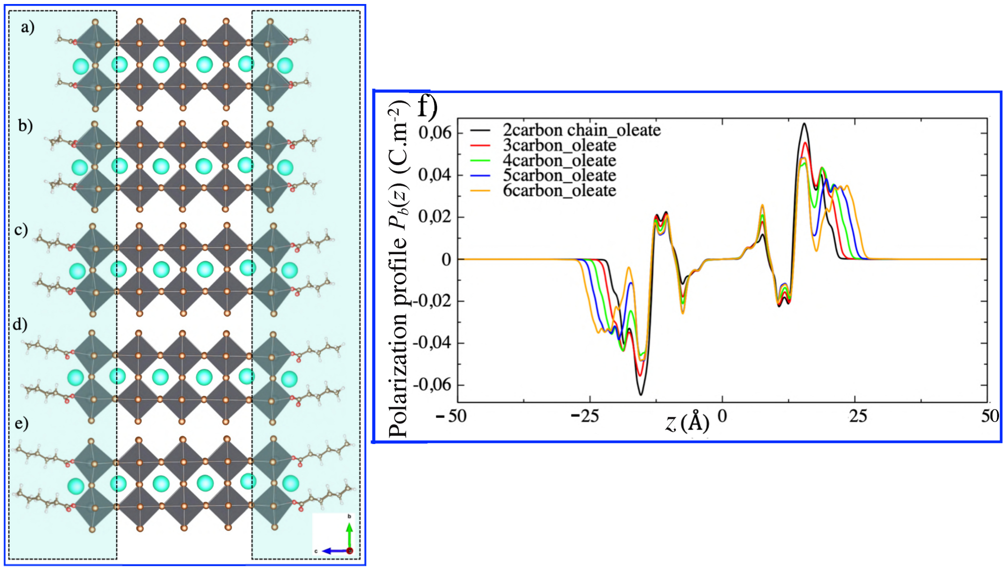

Figure S6: (a)-(e) Relaxed $CsPbBr_3$ model slabs functionalized with oleate anions bearing alkyl chains of various length: from $2-6$ carbons. (f) Corresponding polarization density profiles ($P_b(z)$).

V. Surface energies of CsBr and $PbBr_2$ terminated slabs

We consider a $CsPbBr_3$ slab with a pseudo-cubic structure[11] (vide supra) and start with the CsBr termination, which appears to be more stable as compared to $PbBr_2$ terminated surface[29]. To confirm this, we compare the surface energies of the CsBr and $PbBr_2$ terminated surfaces using the surface bond cleaving (energy required to cut bulk into surfaces) and the relaxation approach to determine the surface energies of the two terminations. The expression for the surface energies ($E_{surface}$) for the two terminations is given by[30,31]:

$$E_{\text{surface}}\,(A) = E_{\text{cl}} + E_{\text{relaxed}}(A) \tag{4}$$

where, E_{cl} and $E_{relaxed}(A)$ are the bond cleavage energy and the slab surface relaxation energy with A (CsBr or $PbBr_2$) terminations, respectively.

After cleaving the bulk crystal, both the surface terminations appear simultaneously and the cleavage energy tends to distribute in the observed surfaces equally. Hence, we anticipate that cleavage energy remains the same for both of the terminations (CsBr or $PbBr_2$).

$$E_{cl} = \frac{1}{4S}\left[E_{slab}^{unrel}(CsBr) + E_{slab}^{unrel}(PbBr_2) - \frac{N_{slab}^{atom}(CsBr) + N_{slab}^{atom}(PbBr_2)}{N_{bulk}^{atom}}E_{bulk}\right] \tag{5}$$

Here, the factor $\frac{1}{4}$ is due to the two symmetric surface slab models that lead to a total of four surfaces to be exposed. S is the surface area of the slab. $E_{slab}^{unrel}(CsBr)$, $E_{slab}^{unrel}(PbBr_2)$, and E_{bulk} are the total energy of unrelaxed CsBr terminated slab, unrelaxed $PbBr_2$ terminated slab, and bulk, respectively. $N_{slab}^{atom}(CsBr)$, $N_{slab}^{atom}(PbBr_2)$ and N_{bulk}^{atom} are the total number of atoms i.e. 42 in slab model with CsBr termination, 38 atoms in $PbBr_2$ termination, and 5 atoms in bulk unit cell, respectively.

The relaxation energies for both the terminations (CsBr and $PbBr_2$) are given by:

$$E_{relaxed}(A) = \frac{1}{2S}\left[E_{slab}(S) - E_{slab}^{(unrel)}(A)\right] \tag{6}$$

where $E_{slab}(A)$ and $E_{slab}^{(unrel)}(A)$ are the slab energy after and before relaxation, respectively. The calculated $E_{surface}(A)$ values reported in Table S4 for the CsBr and $PbBr_2$ terminated surfaces reflect the enhanced stability of CsBr terminated surface over $PbBr_2$ terminated one.

Table S4: Calculated bond cleaving energy (E_{cl}), surface relaxation energies ($E_{relaxed}(A)$) and surface energies ($E_{surface}(A)$) of CsBr and $PbBr_2$ terminated $CsPbBr_3$ slabs.

Structures	E_{cl}(meV/Å^2)	$E_{relaxed}$(meV/Å^2)	$E_{surface}$ (meV/Å^2)
CsBr terminated	16.32	-2.45	13.87
$PbBr_2$ terminated	16.32	-0.56	15.76

VI. Polarization density profile for phosphonate anion on a $CsPbBr_3$ surface

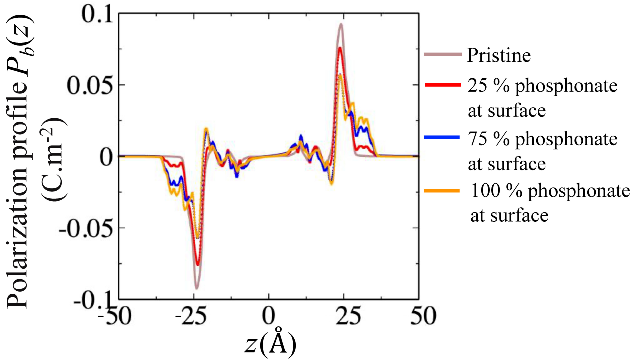

Figure S7: Polarization density profile ($P_b(z)$) for phosphonate anion on a $CsPbBr_3$ surface. The concentration of phosphonate anion varies from 25% to 100%.

VII. Surface relaxation effect on valence levels

a) $CsPbBr_3$ slab with phosphonate anions:

Table S5: Average in-plane Pb-Br-Pb angle and out-of-plane (δ[28]) angle, in-plane and out-of-plane PbBr bond lengths at the outermost surface layers of $CsPbBr_3$ slabs functionalized with phosphonate anions. The molecular concentration on the surface varies from $25\%to100\%$. Subscripts ”in” and ”out” refer to the in-plane and out-of-plane, respectively.

	$PbBr_{in}$ (Å)	Pb-Br-Pb_{in} (°)	$PbBr_{out}$ (Å)	δ_{out} (°)
25%	3.06	166.8	3.05	3.32
50%	3.04	172.0	3.07	0.74
75%	3.04	171.5	3.08	0.66
100%	3.04	171.1	3.09	0.64

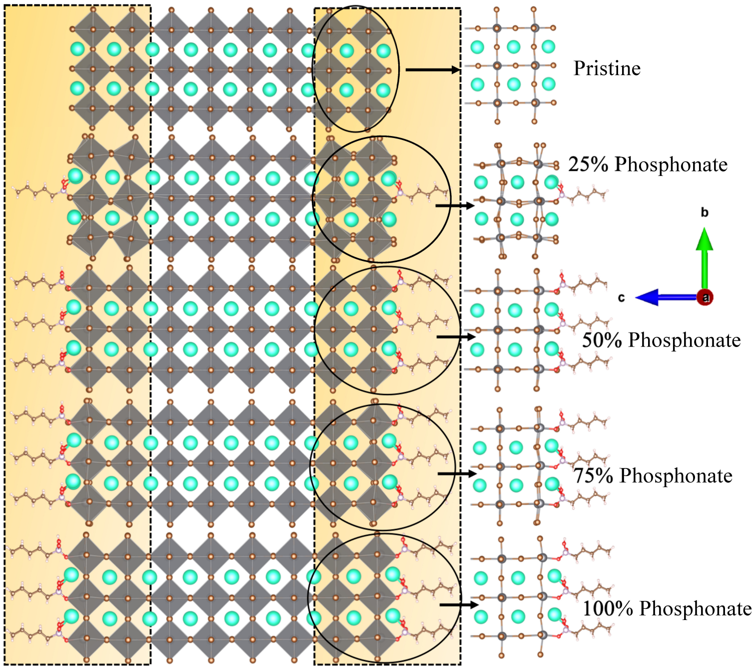

Figure S8: Relaxed $CsPbBr_3$ CsBr terminated slabs without (pristine) and with phosphonate ligands attached to the surface. The concentration of phosphonate anions varies from 25% to 100%. Note that the visualization of the repetition of molecules at the surface boundary (for 50%, 75% and 100%) is the way the VESTA software shows the structure due to periodic boundary conditions.

We examine here the interplay of octahedra distortions of the surface layer and contraction or expansion of PbBr bond lengths at the surface. For a coverage of 25%, we observe from Table S5 that the surface layers are more distorted compared to higher concentrations, with smaller in-plane Pb-Br-Pb angles and larger out of plane delta (δ) angles. It is well known that octahedral distortions influence the electronic properties significantly. These larger deviations in bond angles (Pb-Br-Pb) at the surface contribute to the relative deeper valence level position.

b) $CsPbBr_3$ slab with oleate anions:

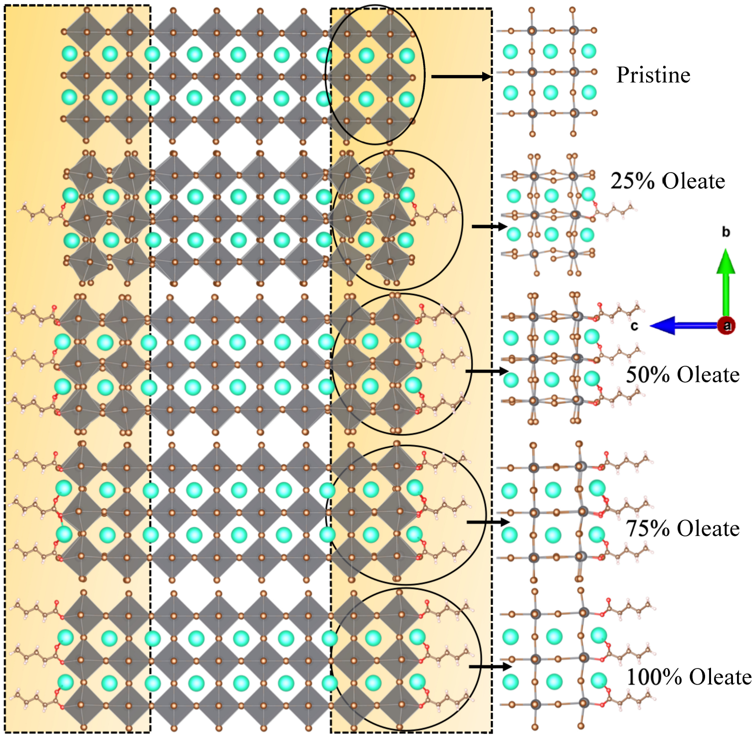

Figure S9: Relaxed $CsPbBr_3$ CsBr terminated slabs without (pristine) and with oleate ligands attached to the surface. The concentration of oleate anions varies from 25% to 100%. Note that the visualization of the repetition of molecules at the surface boundary (for 50%, 75% and 100%) is the way the VESTA software shows the structure due to periodic boundary conditions.

Table S6: Average in-plane Pb-Br-Pb angle and out-of-plane (δ angle[28]), in-plane and out-of-plane PbBr bond lengths at the outermost surface layers of $CsPbBr_3$ slab functionalized with oleate anion. The concentration varies from $25\%to100\%$. Subscripts "in" and "out" refer to the in-plane and out-of-plane, respectively.

	$PbBr_{in}$ (Å)	Pb-Br-Pb_{in} (°)	$PbBr_{out}$ (Å)	δ_{out} (°)
25%	3.06	167.1	3.06	5.20
50%	3.05	171.3	3.08	3.37
75%	3.04	173.3	3.09	0.77
100%	3.04	172.4	3.11	0.52

Like phosphonate, at a coverage of 25%, the surface layers are more distorted with smaller in-plane Pb-Br-Pb angles and larger out of plane delta (δ) angles. The larger deviation in bond angles (Pb-Br-Pb) at 25% coverage results in a deeper valence level compared to 50%, 75%, and 100% coverage. Between 75% and 100% concentration, there is only a slight change in the bond length and bond angles of the outermost surface layer, therefore valence energies do not change significantly ($\sim$ 0.04 eV (Fig S11(b))), and approach almost saturation at 75% concentration.

c) CsPbBr$_3$ slab with DMSO:

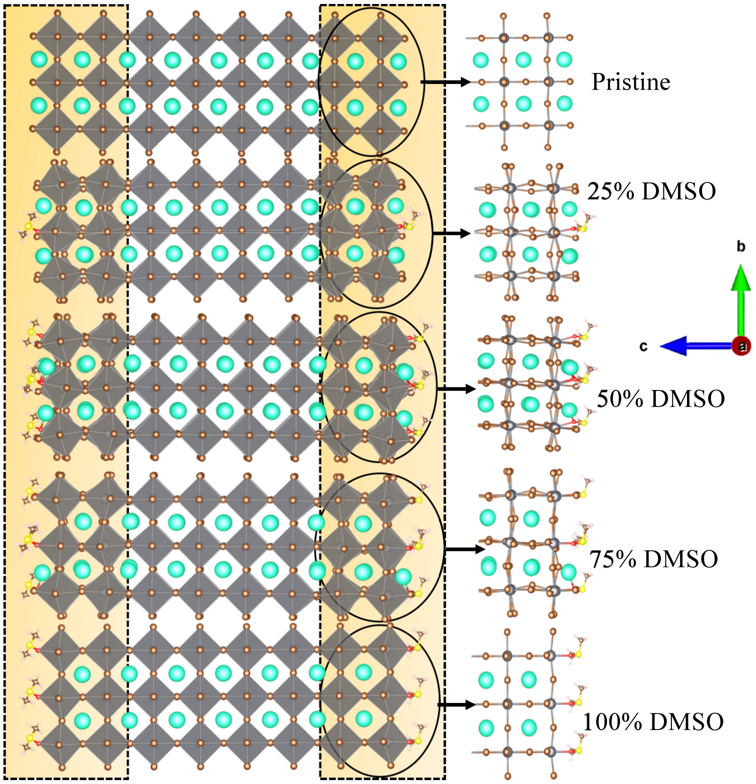

Figure S10: Relaxed CsPbBr$_3$ CsBr terminated slabs without (pristine) and with DMSO ligands attached to the surface. The concentration of DMSO anions varies from 25% to 100%. Note that the visualization of the repetition of molecules at the surface boundary (for 50%, 75% and 100%) is the way the VESTA software shows the structure due to periodic boundary conditions.

Table S7: Average in-plane Pb-Br-Pb angle and out-of-plane (δ angle^{28}), in-plane and out-of-plane PbBr bond lengths at the outermost surface layers of CsPbBr$_3$ slab functionalized with DMSO. The concentration varies from $25\% to 100\%$. Subscripts "in" and "out" refer to the in-plane and out-of-plane, respectively.

	PbBr$_{in}$ (Å)	Pb-Br-Pb$_{in}$ (°)	PbBr$_{out}$ (Å)	δ_{out} (°)
25%	3.08	162.3	3.05	5.89
50%	3.08	160.5	3.05	5.77
75%	3.08	162.0	3.05	5.47
100%	3.05	168.4	3.05	0.69

Unlike phosphonate and oleate anions, between 75% and 100% coverage, a noticeable change of bond angles of the outermost surface layer is observed, which contributes to the change in valence energy ($\sim$ 0.5 eV, (FigS11 (d), compared to FigS11 (b)). We notice that among phosphonate, oleate and DMSO, the octahedral distortions of the surface layer and contraction or expansion of PbBr bond lengths are more prominent in DMSO. This results from the larger dipole moment (Table 1) and reduced steric hindrance of DMSO (Figure S10) as compared to the other two investigated ligands (Figure S8 and S9).

d) $CsPbBr_3$ slab with anilinium derivatives:

Table S8: Average in-plane Pb-Br-Pb angle and out-of-plane (δ angle[28]), in-plane and out-of-plane PbBr bond lengths at the outermost surface layers of $CsPbBr_3$ slab functionalized with anilinium-OCH_3, anilinium, and anilinium-NO_2 for a surface coverage of 25%. Subscripts "in" and "out" refer to the in-plane and out-of-plane, respectively.

	$PbBr_{in}$ (Å)	Pb-Br-Pb_{in} (°)	$PbBr_{out}$ (Å)	δ_{out} (°)
25% anilinium$-OCH_3$	3.07	162.3	3.05	5.86
25% anilinium	3.08	161.3	3.05	5.89
25% anilinium$-NO_2$	3.09	157.3	3.05	7.27

At 25% concentration, the surface layers of anilinium$-NO_2$ are more distorted than those of anilinium and anilinium-OCH_3, given the smaller in-plane Pb-Br-Pb angles and larger out of plane delta (δ) angles (Table S8). This is again correlated with a larger dipole moment (Table 1), but with opposite orientation as compared to DMSO, and in turn leads to deeper valence levels.

e) $CsPbBr_3$ slab with DA, DDA and DMDDA:

To gauge at a first approximation effect of finite temperature, we extracted structural information from snapshots obtained using classical MD simulations performed at ambient conditions for the alkylammonium ligands grafted on the surface of perovskite nanocrystals[20]. Structural information related to octahedral distortions are summarized in Table S9. When going from primary to quaternary ammonium, in-plane octahedral tilting is only slightly reduced in favor of out-of-plane tilting, whereas the outer Pb-Br bond length is moderately reduced.

Table S9: Average in-plane Pb-Br-Pb angle and out-of-plane (δ angle[28]), in-plane and out-of-plane PbBr bond lengths extracted from snapshots of classical MD simulations at ambient conditions[20]. Values in parentheses report the data obtained from DFT optimization of surface with ligands on our model slabs. Subscripts "in" and "out" refer to the in-plane and out-of-plane, respectively.

	$PbBr_{in}$ (Å)	Pb-Br-Pb_{in} (°)	$PbBr_{out}$ (Å)	δ_{out} (°)
DA	2.93 (2.97)	171.7 (161.1)	2.97 (2.97)	7.02 (7.22)
DDA	2.93 (2.97)	171.1 (160.7)	2.89 (2.97)	7.74 (7.99)
DMDDA	2.96 (2.97)	170.6 (162.5)	2.88 (2.97)	9.11 (7.00)

VIII. Oleate anion and DMSO molecule on a $CsPbBr_3$ surface

With increase in concentration of oleate anion at the surface, a continuous increase in the valence energy is observed. The calculated valence energies for 0%, 25%, 50%, 75% and 100% are given in Fig S11(b) and Table 2. Between 75% and 100% concentration, the E_v^{abs} value does not change significantly ($\sim$ 0.04 eV). The corresponding polarization density profiles ($P_b(z)$) shown in Fig S11(c) infer a continuous reduction of the surface dipole with the increase in the concentration of oleate. Therefore, we conclude that the increase in E_v^{abs} for oleate is induced by the reduction of surface dipole density, which is positive, as a result of charge transfer from oleate to the outer perovskite layer, implying a dipole direction away from the CsBr slab Fig S11(f).

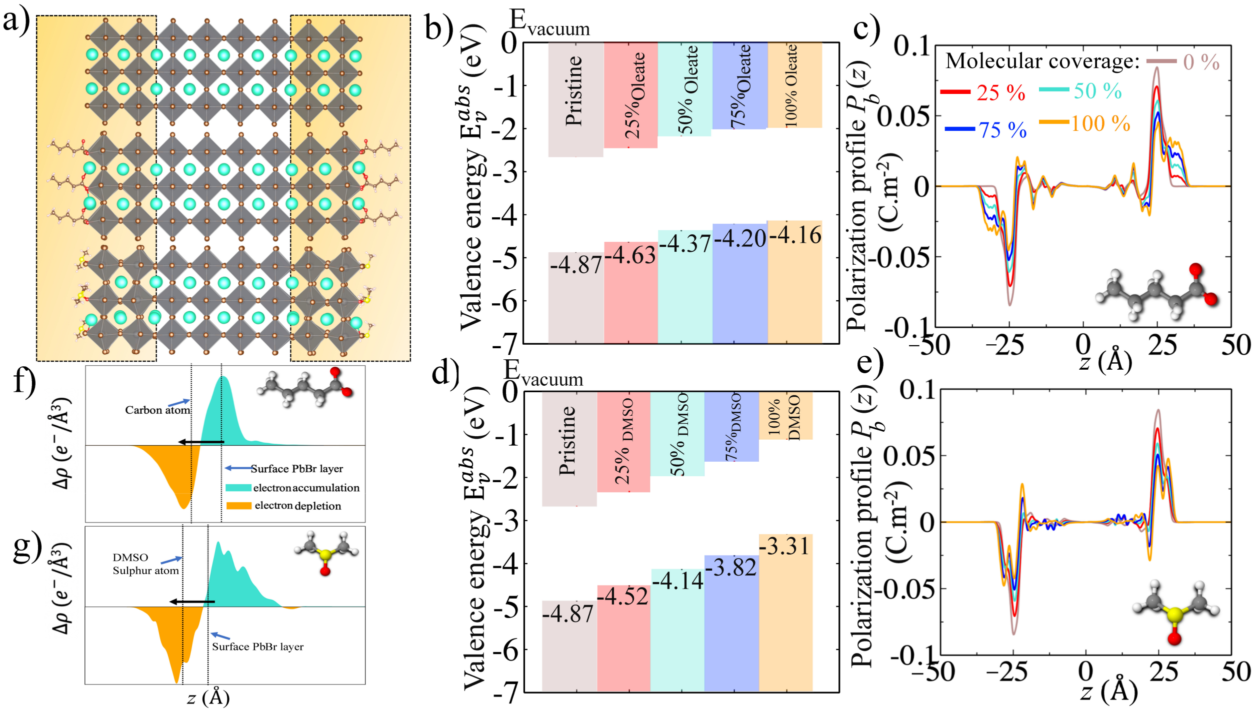

Figure S11: a) $CsPbBr_3$ CsBr terminated slabs without (top) and with (bottom) oleate and DMSO ligands attached to the surface. The later are illustrated for 50% molecular coverage. For various concentration of oleate anions, computed b) valence energies and c) polarization density profiles. For various concentration of DMSO, computed d) valence energies and e) polarization density profiles. Profiles of electronic charge density difference for slabs functionalized with f) oleate or g) DMSO ligands for a molecular coverage of 50%. For clarity, only one side of the symmetric slab is shown. Orange and turquoise color represent electronic depletion and accumulation region, respectively, and the arrow indicates the net dipole direction.

When using DMSO, from Fig S11(d) we notice a continuous increase in the valence energies (E_v^{abs}) with increasing coverage. The corresponding E_v^{abs} computed from Hartree potential alignments are given in Table 2. This corroborates that increase in E_v^{abs} for DMSO is attributed to the decrease of the surface dipole density (from $P_b(z)$ profiles, Fig S11(e)) as a result of surface functionalization. The decrease in the surface dipole density can be further attributed to electron transfer from DMSO to the outer perovskite layer yielding a dipole direction away from the surface Fig S11(g).

Variation of surface dipole densities (Δp) and valence energies (ΔE_v^{abs}) as a function of molecular coverage present a linear behavior, with a tendency to saturate for oleate anion from 75% to 100% (Fig S12). This effect is attributed to additional strain effects due to the bulky nature of the oleate anion.

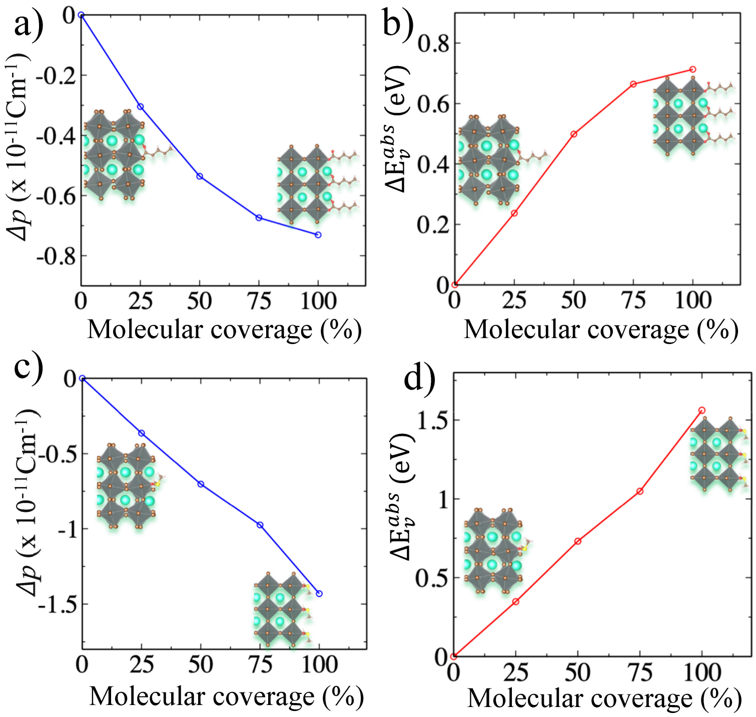

Figure S12: Relation between the change in surface dipole density and the molecular coverage for $CsPbBr_3$ slabs functionalized with a) oleate and c) DMSO ligands. Corresponding variation of valence energy in panel b) and d), respectively.

IX. Band structure of $CsPbBr_3$ slabs with phosphonate, oleate and DMSO ligands

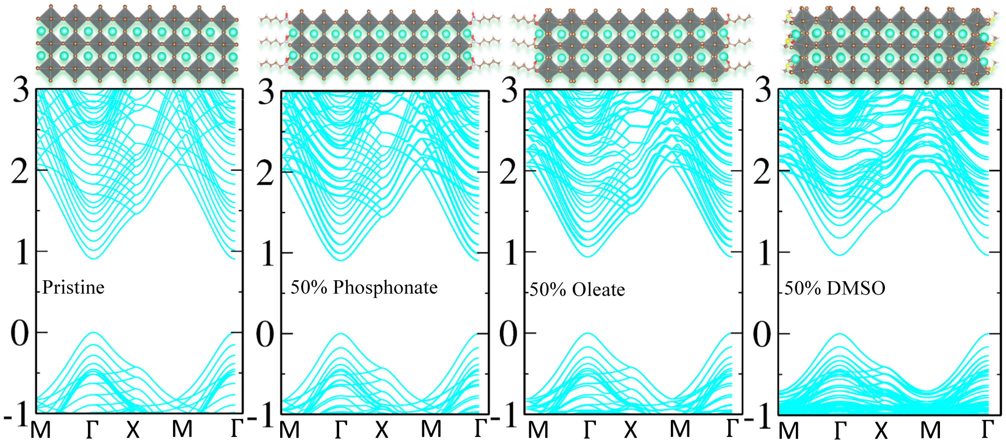

Figure S13: Band structure of $CsPbBr_3$ slabs functionalized with phosphonate, oleate and DMSO at 50% concentration computed at the PBE+SOC level of theory.

X. Band structure of $CsPbBr_3$ slabs with anilinium and its derivatives

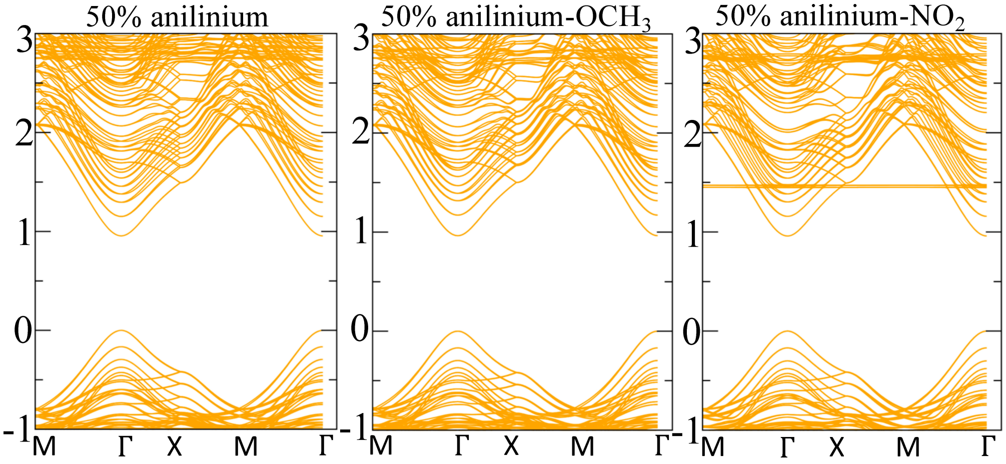

Figure S14: Band structure of $CsPbBr_3$ slabs functionalized with anilinium and its derivatives computed at the PBE+SOC level of theory.

XI. Experimental valence energy positions of aniline, aniline$-$OCH$_3$ and aniline$-$NO$_2$-treated perovskite films[1]

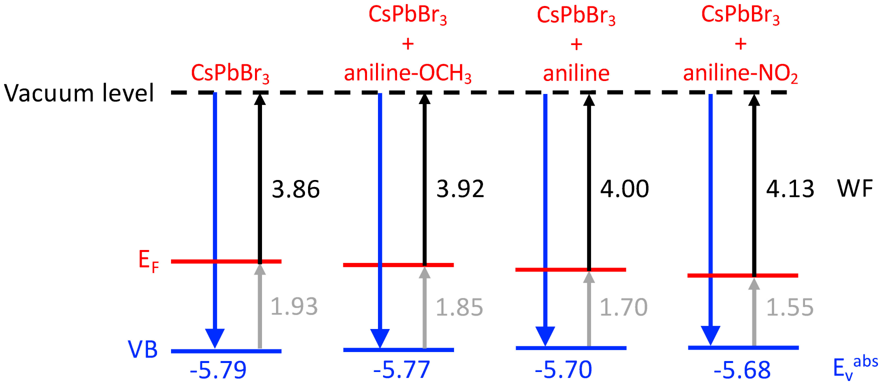

Figure S15: Valence energies extracted from Ref.[1]. The work function of control, $-$OCH$_3$, aniline, and $-$NO$_2$-treated perovskite films were obtained from the UPS spectra[1].

XII. $CsPbBr_3$ slabs with aniline and its derivatives, with the NH_2 group pointing towards the perovskite surface

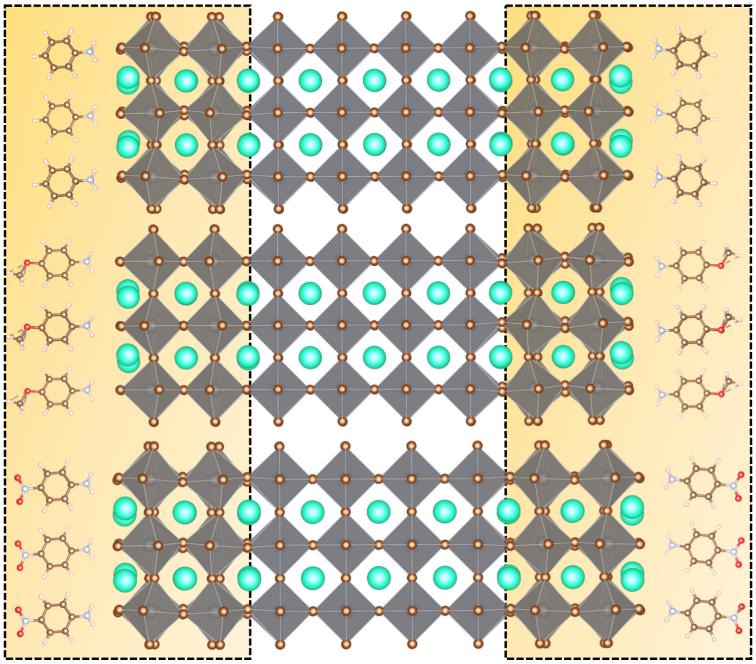

Figure S16: Relaxed $CsPbBr_3$ CsBr terminated slabs with aniline (top), aniline$-OCH_3$ (middle) and aniline$-NO_2$ (bottom) ligands coated on the outer surface of the slab, with the $-NH_2$ group pointing towards the surface.

Table S10: Valence energies (E_v^{abs}) calculated at the PBE+SOC level of theory for different molecules with molecular coverage varying from 0% − 100% for a CsBr terminated $CsPbBr_3$ slab. Shifts of valence levels obtained from the approach based on the Hartree potential alignment ΔE_v^{abs}[HP] (Fig S3(d)) and from the difference of surface dipole density (ΔE_v^{abs}) using Eq 9.

Relaxed CsBr terminated slab				
	E_v^{abs} (eV)	ΔE_v^{abs} [HP] (eV)	$\Delta p \times 10^{-11}$ (C/m)	ΔE_v^{abs} (eV) [Eq 9]
$CsPbBr_3$ slab with aniline				
Pristine	− 4.87	-	-	-
25% aniline	− 5.27	− 0.40	+ 0.27	− 0.31
50% aniline	− 5.52	− 0.65	+ 0.49	− 0.55
75% aniline	− 5.61	− 0.74	+ 0.57	− 0.64
100% aniline	− 5.72	− 0.85	+ 0.64	− 0.72
$CsPbBr_3$ slab with aniline$-OCH_3$				
Pristine	−4.87	-	-	-
25% aniline$-OCH_3$	−5.09	− 0.22	+ 0.10	− 0.11
50% aniline$-OCH_3$	− 5.13	− 0.26	+ 0.13	− 0.15
$CsPbBr_3$ slab with aniline$-NO_2$				
Pristine	−4.87	-	-	-
25% aniline$-NO_2$	− 6.48	− 1.61	+ 1.35	− 1.53
50% aniline$-NO_2$	− 7.53	− 2.66	+ 2.28	− 2.57
75% aniline$-NO_2$	− 8.15	− 3.28	+ 2.81	− 3.18
100% aniline$-NO_2$	−8.59	−3.72	+ 3.17	− 3.58

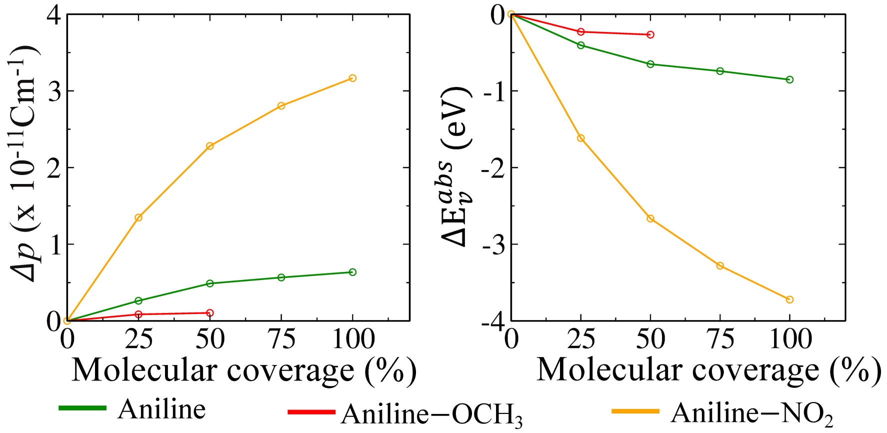

Figure S17: Relation between the change in surface dipole density and the molecular coverage (left panel) for $CsPbBr_3$ slabs functionalized with aniline, aniline$-OCH_3$ and aniline$-NO_2$. Relation between the change in the valence energies and the molecular coverage (right panel) for $CsPbBr_3$ slabs functionalized with aniline, aniline$-OCH_3$ and aniline$-NO_2$.

XIII. Aniline$-NO_2$ with the NO_2 group pointing towards the perovskite surface

Interestingly, with the NO_2 group pointing towards the perovskite surface, the valence levels undergoes an upward shift (Table S11). But, at the smallest computed coverage (25%), this shift is predicted to be huge, whereas the experimental one is about 0.1 eV[1].

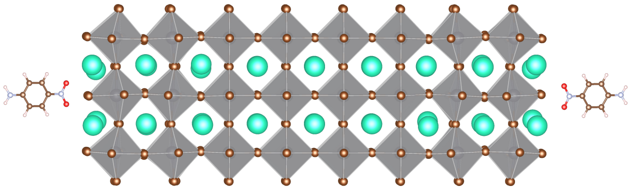

Figure S18: Relaxed $CsPbBr_3$ CsBr terminated slabs with 25% coverage of aniline$-NO_2$, where the NO_2 group is pointing towards the perovskite surface. Notably, the modeling strategy which is shown here is only one of the possibilities. Ligands such as aniline$-NO_2$ are also expected to interact through interactions between the nitro group and the metal cations.

Table S11: Valence energies (E_v^{abs}) calculated at the PBE+SOC level of theory for aniline$-NO_2$, with the NO_2 group pointing towards the surface and 25% molecular coverage, for a CsBr terminated $CsPbBr_3$ slab. Shifts of valence levels obtained from the approach based on the Hartree potential alignment ΔE_v^{abs}[HP] (Fig S3(d)) and from the difference of surface dipole density (ΔE_v^{abs}) using Eq 9.

	E_v^{abs} (eV)	ΔE_v^{abs} [HP] (eV)	$p \times 10^{-11}$ (C/m)	$\Delta p \times 10^{-11}$ (C/m)	ΔE_v^{abs} (eV) [Eq 9]
Pristine	-4.86	–	$+3.50$	–	–
25% Aniline$-NO_2$	-3.20	$+1.66$	$+2.00$	-1.50	$+1.69$

Based on the overall discussions above, it can be concluded that the attachment of a molecular site (either electron-rich or electron-poor) to the surface plays a crucial role. The direction of the molecular ligands determines the direction of the dipole, which preconditions how charge is transferred across the surface. The latter has a significant effect on the surface charge and dipolar densities. Our observations indicate that when the electron-rich region is positioned towards the perovskite surface (refer to Fig 1 and Fig S4 for visualizing electron-rich and electron-poor regions), we observe upward shifts in the valence levels. This trend is observed in cases such as

DMSO, oleate, and phosphonate (Table 2). Conversely, in the case of nitroaniline, where the NH_2 group (electron-poor region) points towards the perovskite surface, we observe downward shifts in the valence levels (Table S10). However, by changing the orientation and rotating the NO_2 group (an electron-rich region) towards the perovskite surface, we anticipate an upward shift of the valence levels, which is indeed observed in our results (Table S11).

XIV. Band structure of $CsPbBr_3$ slabs functionalized with aniline and its derivatives

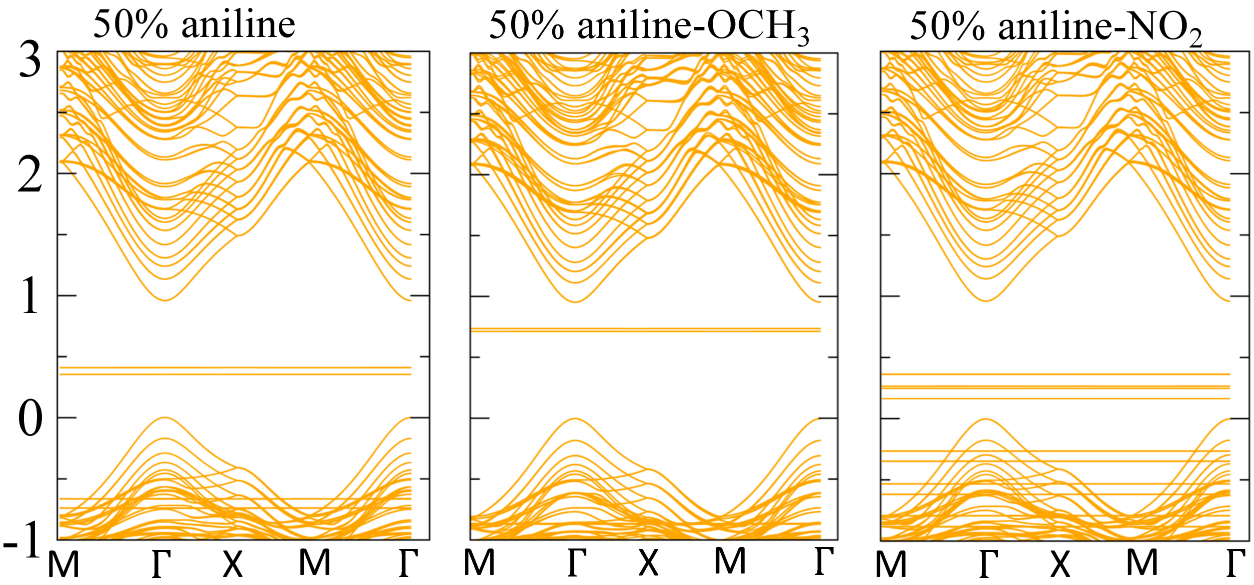

Figure S19: Band structure of $CsPbBr_3$ slabs functionalized with aniline and its derivatives at the PBE+SOC level of theory.

XV. Additivity of surface dipole densities and electric susceptibilities

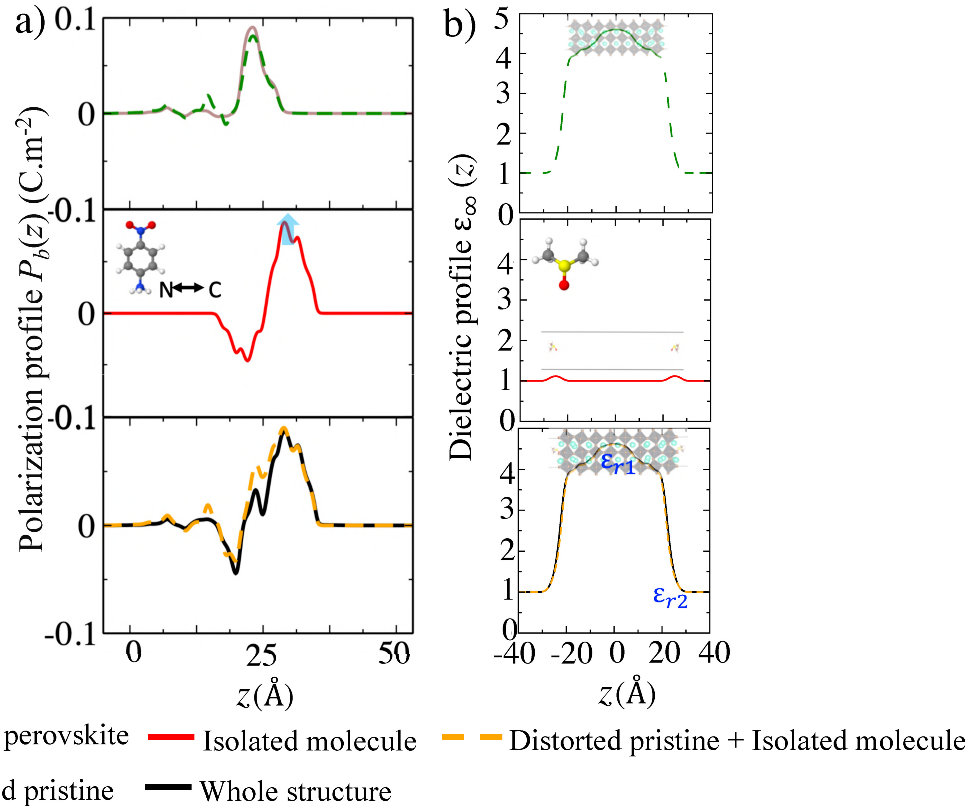

Figure S20: a) Additivity of surface dipole densities illustrated with the plot of the polarization density profiles ($P_b(z)$) computed for a $CsPbBr_3$ slab functionalized with anilinium$-NO_2$, where the NH_3^+ group substitutes a Cs-atom of the outer layer. Notably, anilinium$-NO_2$ is a charged molecule, and our methodology works for neutral systems, therefore we perform a computational trick by replacing the nitrogen (N^+) with carbon (C). b) Additivity of electric susceptibilities for $CsPbBr_3$ slabs functionalized with DMSO.

XVI. Dielectric constant at the position of the molecules

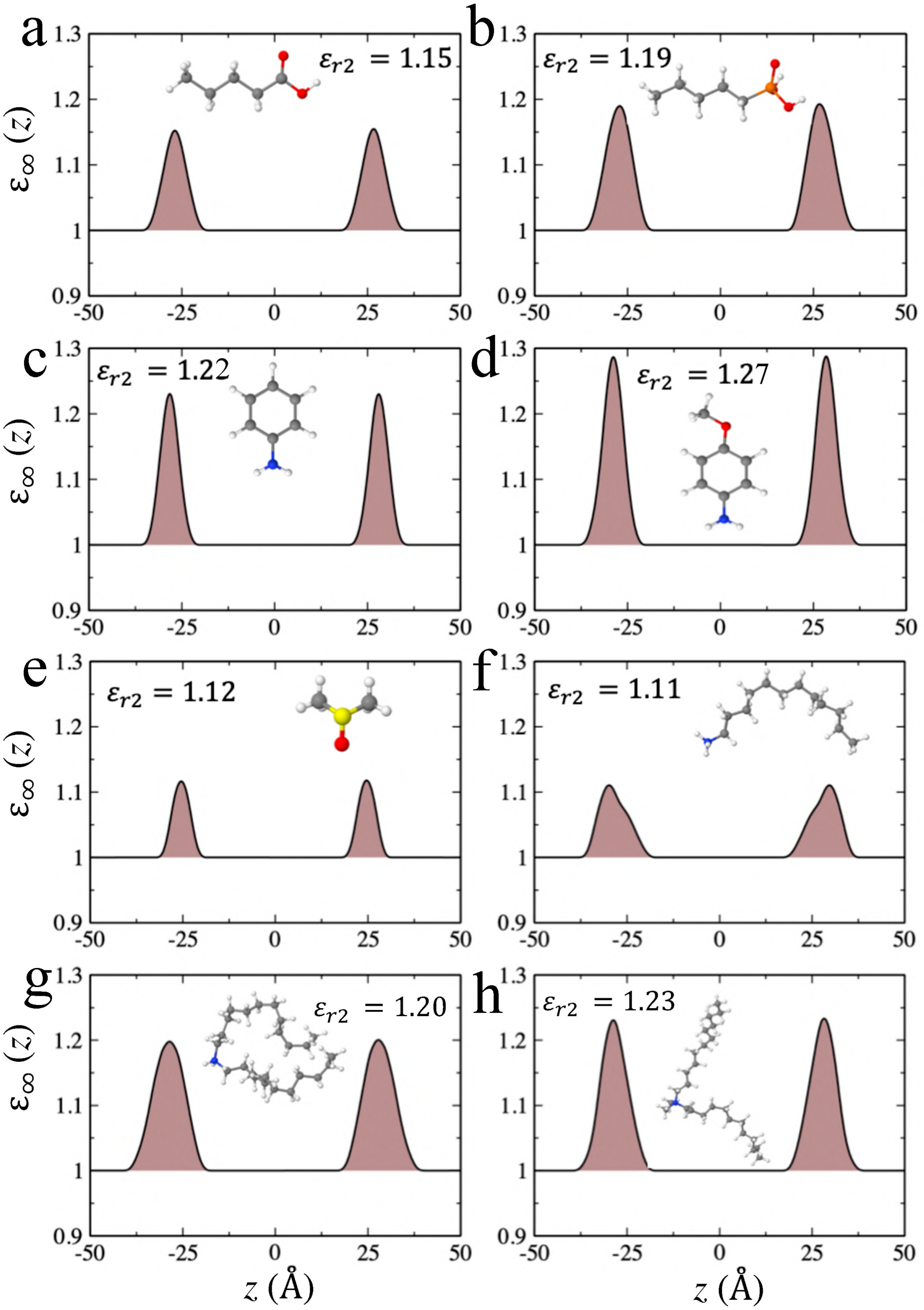

Figure S21: Computed position dependent high frequency dielectric profiles and corresponding dielectric constant at the position of the molecules for a) oleic acid, b) phosphonic acid, c) aniline, d) aniline−OCH$_3$, e) DMSO, f) primary dodecylammonium (DA), g) secondary didodecylammonium (DDA), and h) quaternary dimethyldidodecylammonium (DMDDA).

References

(1) Duan, J.; Wang, M.; Wang, Y.; Zhang, J.; Guo, Q.; Zhang, Q.; Duan, Y.; Tang, Q. Effect of side-group-regulated dipolar passivating molecules on $CsPbBr_3$ perovskite solar cells. *ACS Energy Letters* **2021**, *6*, 2336–2342.

(2) Soler, J. M.; Artacho, E.; Gale, J. D.; García, A.; Junquera, J.; Ordejón, P.; Sánchez-Portal, D. The SIESTA method for ab initio order-N materials simulation. *Journal of Physics: Condensed Matter* **2002**, *14*, 2745.

(3) Artacho, E.; Anglada, E.; Diéguez, O.; Gale, J. D.; García, A.; Junquera, J.; Martin, R. M.; Ordejón, P.; Pruneda, J. M.; Sánchez-Portal, D. et al. The SIESTA method; developments and applicability. *Journal of Physics: Condensed Matter* **2008**, *20*, 064208.

(4) Hohenberg, P.; Kohn, W. Inhomogeneous electron gas. *Physical review* **1964**, *136*, B864.

(5) Kohn, W.; Sham, L. J. Self-consistent equations including exchange and correlation effects. *Physical review* **1965**, *140*, A1133.

(6) Cooper, V. R. Van der Waals density functional: An appropriate exchange functional. *Physical Review B* **2010**, *81*, 161104.

(7) Bitzek, E.; Koskinen, P.; Gähler, F.; Moseler, M.; Gumbsch, P. Structural relaxation made simple. *Physical review letters* **2006**, *97*, 170201.

(8) Troullier, N.; Martins, J. L. Efficient pseudopotentials for plane-wave calculations. *Physical review B* **1991**, *43*, 1993.

(9) García-Gil, S.; García, A.; Lorente, N.; Ordejón, P. Optimal strictly localized basis sets for noble metal surfaces. *Physical Review B* **2009**, *79*, 075441.

(10) Perdew, J. P.; Burke, K.; Ernzerhof, M. Generalized gradient approximation made simple. *Physical review letters* **1996**, *77*, 3865.

(11) Stoumpos, C. C.; Malliakas, C. D.; Peters, J. A.; Liu, Z.; Sebastian, M.; Im, J.; Chasapis, T. C.; Wibowo, A. C.; Chung, D. Y.; Freeman, A. J. et al. Crystal growth of the perovskite semiconductor $CsPbBr_3$: a new material for high-energy radiation detection. *Crystal growth & design* **2013**, *13*, 2722–2727.

(12) Bengtsson, L. Dipole correction for surface supercell calculations. *Physical Review B* **1999**, *59*, 12301.

(13) Meyer, B.; Vanderbilt, D. Ab initio study of $BaTiO_3$ and $PbTiO_3$ surfaces in external electric fields. *Physical Review B* **2001**, *63*, 205426.

(14) Ferreira, L. G.; Marques, M.; Teles, L. K. Approximation to density functional theory for the calculation of band gaps of semiconductors. *Physical Review B* **2008**, *78*, 125116.

(15) Tao, S. X.; Cao, X.; Bobbert, P. A. Accurate and efficient band gap predictions of metal halide perovskites using the DFT-1/2 method: GW accuracy with DFT expense. *Scientific reports* **2017**, *7*, 1–9.

(16) Traoré, B.; Even, J.; Pedesseau, L.; Kepenekian, M.; Katan, C. Band gap, effective masses, and energy level alignment of 2D and 3D halide perovskites and heterostructures using DFT-1/2. *Physical Review Materials* **2022**, *6*, 014604.

(17) Even, J.; Pedesseau, L.; Dupertuis, M.-A.; Jancu, J.-M.; Katan, C. Electronic model for self-assembled hybrid organic/perovskite semiconductors: Reverse band edge electronic states ordering and spin-orbit coupling. *Physical Review B* **2012**, *86*, 205301.

(18) Das, T.; Rocquefelte, X.; Jobic, S. Ab Initio Positioning of the Valence and Conduction Bands of Bulk Photocatalysts: Proposition of Absolute Reference Energy. *The Journal of Physical Chemistry C* **2020**, *124*, 19426–19434.

(19) Lodeiro, L.; Barría-Cáceres, F.; Jiménez, K.; Contreras, R.; Montero−Alejo, A. L.; Menéndez-Proupin, E. Methodological issues in first-principle calculations of $CH_3NH_3PbI_3$

perovskite surfaces: quantum confinement and thermal motion. *ACS omega* **2020**, *5*, 29477–29491.

(20) Stelmakh, A.; Aebli, M.; Baumketner, A.; Kovalenko, M. V. On the mechanism of alkylammonium ligands binding to the surface of $CsPbBr_3$ nanocrystals. *Chemistry of Materials* **2021**, *33*, 5962–5973.

(21) Ahn, N.; Son, D.-Y.; Jang, I.-H.; Kang, S. M.; Choi, M.; Park, N.-G. Highly reproducible perovskite solar cells with average efficiency of 18.3% and best efficiency of 19.7% fabricated via Lewis base adduct of lead (II) iodide. *Journal of the American Chemical Society* **2015**, *137*, 8696–8699.

(22) Vidal, R.; Alberola-Borràs, J.-A.; Habisreutinger, S. N.; Gimeno-Molina, J.-L.; Moore, D. T.; Schloemer, T. H.; Mora-Seró, I.; Berry, J. J.; Luther, J. M. Assessing health and environmental impacts of solvents for producing perovskite solar cells. *Nature Sustainability* **2021**, *4*, 277–285.

(23) Petrov, A. A.; Fateev, S. A.; Khrustalev, V. N.; Li, Y.; Dorovatovskii, P. V.; Zubavichus, Y. V.; Goodilin, E. A.; Tarasov, A. B. Formamidinium haloplumbate intermediates: the missing link in a chain of hybrid perovskites crystallization. *Chemistry of Materials* **2020**, *32*, 7739–7745.

(24) Cao, J.; Jing, X.; Yan, J.; Hu, C.; Chen, R.; Yin, J.; Li, J.; Zheng, N. Identifying the molecular structures of intermediates for optimizing the fabrication of high-quality perovskite films. *Journal of the American Chemical Society* **2016**, *138*, 9919–9926.

(25) Nenon, D. P.; Pressler, K.; Kang, J.; Koscher, B. A.; Olshansky, J. H.; Osowiecki, W. T.; Koc, M. A.; Wang, L.-W.; Alivisatos, A. P. Design principles for trap-free $CsPbX_3$ nanocrystals: enumerating and eliminating surface halide vacancies with softer Lewis bases. *Journal of the American Chemical Society* **2018**, *140*, 17760–17772.

(26) Kazes, M.; Udayabhaskararao, T.; Dey, S.; Oron, D. Effect of surface ligands in perovskite

nanocrystals: extending in and reaching out. *Accounts of Chemical Research* **2021**, *54*, 1409–1418.

(27) Ravi, V. K.; Santra, P. K.; Joshi, N.; Chugh, J.; Singh, S. K.; Rensmo, H.; Ghosh, P.; Nag, A. Origin of the substitution mechanism for the binding of organic ligands on the surface of CsPbBr3 perovskite nanocubes. *The Journal of Physical Chemistry Letters* **2017**, *8*, 4988–4994.

(28) Pedesseau, L.; Sapori, D.; Traore, B.; Robles, R.; Fang, H.-H.; Loi, M. A.; Tsai, H.; Nie, W.; Blancon, J.-C.; Neukirch, A. et al. Advances and promises of layered halide hybrid perovskite semiconductors. *ACS nano* **2016**, *10*, 9776–9786.

(29) Bodnarchuk, M. I.; Boehme, S. C.; Ten Brinck, S.; Bernasconi, C.; Shynkarenko, Y.; Krieg, F.; Widmer, R.; Aeschlimann, B.; Gu nther, D.; Kovalenko, M. V. et al. Rationalizing and controlling the surface structure and electronic passivation of cesium lead halide nanocrystals. *ACS energy letters* **2018**, *4*, 63–74.

(30) Heifets, E.; Eglitis, R.; Kotomin, E.; Maier, J.; Borstel, G. Ab initio modeling of surface structure for $SrTiO_3$ perovskite crystals. *Physical Review B* **2001**, *64*, 235417.

(31) Eglitis, R. I. Ab initio hybrid DFT calculations of $BaTiO_3$, $PbTiO_3$, $SrZrO_3$ and $PbZrO_3$ (111) surfaces. *Applied Surface Science* **2015**, *358*, 556–562.